Direction-of-Arrival Estimation in Closely Distributed Array Exploiting Mixed-Precision Covariance Matrices

Yimin D. Zhang and Md Waqeeb T. S. Chowdhury

Abstract

In this paper, we explore a collaborative direction-of-arrival (DOA) estimation technique that utilizes multiple closely spaced subarrays to maximize the potential of distributed arrays while minimizing communication overhead between the subarrays and the processing center. Each subarray computes its self-covariance matrix using the full-precision data and transmits it, along with a one-bit version of the measured data, to the processing center. The processing center generates one-bit cross-covariance matrices between subarrays, which are combined with full-precision subarray self-covariance matrices to create the mixed-precision covariance matrix of the entire array for source DOA estimation. This approach utilizes the full array aperture and all available degrees of freedom of the entire distributed array. To address missing entries in the full covariance matrix, we employ matrix completion, taking into account its Toeplitz and Hermitian structure. For subarrays that are not positioned on the half-wavelength grid, we propose an iterative DOA estimation method to ensure robust DOA estimation performance. Our proposed approach outperforms scenarios where cross-covariance matrices are unavailable or the entire covariance matrix is not interpolated. With the same communication traffic limitation, it demonstrates superiority over schemes that utilize only full-precision data or only one-bit data.

**The authors are with the Department of Electrical and Computer Engineering, Temple University, Philadelphia, PA 19122, USA (emails: ydzhang@temple.edu, tun62948@temple.edu.)

1. Introduction

Array processing plays an important role in various applications in wireless communications, radar sensing, and radio astronomy [3–5]. Distributed sensor array platforms enabling collaborative sensing and network communication systems are gaining popularity in diverse sensing applications [6–12]. When using a large-scale array is impractical or impossible due to platform limitations, distributed arrays can be an attractive alternative. Distributed arrays are composed of multiple separately separated subarrays with a small number of sensors each. In such platforms, fusing the information observed at multiple distributed subarrays forms a virtual array with a larger aperture, more degrees of freedom (DOFs), and significantly enhanced sensing capability [13–16].

In this paper, we investigate a collaborative platform where multiple distributed subarrays are used to estimate source directions-of-arrival (DOAs). These subarrays are collocated, i.e., while the separation between these subarrays could be larger than the subarray size, they are close enough so that the different subarrays observe each impinging source with the same DOA. Such problems can be encountered in a broad class of distributed array sensing applications involving automotive radar, unmanned aerial vehicles (UAVs) and Internet of Things (IoT), where each vehicle or node is equipped with a small-size array [17, 18]. It is noted that subarrays may have different numbers of sensors and different sensor configurations, such as uniform spacing, sparse spacing with the same configuration, or sparse spacing with different configurations. We consider the general case that the subarrays have the same number of sensors, but the array configuration in each subarray generally differs. Sparse subarray configurations provide better sensing capability as they reduce the redundancy in computing the second-order correlation required for DOA estimation [19–24].

Both coherent and non-coherent approaches can be used to estimate signal DOAs for distributed arrays. Assuming complete subarray synchronization and precise position information for each subarray, coherent DOA estimation is implemented by sending all subarray data to a processing center where

these data are combined to create a virtual full array with a large aperture. The formed array is frequently referred to as a partially calibrated array when the sensor positions within each subarray are correctly calibrated, but the relative positions of the subarrays are unknown. For example, the DOA estimation problem for a partially calibrated array is considered in [14].

Coherent processing of data observed at different subarrays requires several demanding conditions, including transfer of high-volume raw data from the subarrays to the processing center. Such high-volume traffic can be avoided by using the much simpler non-coherent processing strategy [13, 15, 16]. In this case, each subarray computes its covariance matrix locally and forwards it to the processing center. This reduces the communication traffic significantly compared to coherent processing, which requires raw data to be transferred to the processing center. However, non-coherent processing suffers from a substantial loss of array aperture and DOA estimation performance.

In this paper, we propose a novel strategy that achieves high-resolution DOA estimation with low communication traffic. In this scheme, each subarray computes its self-subarray covariance matrix using the full-precision measured data. For brevity, we refer to the covariance matrix of the subarray signal vector as self-covariance matrix, whereas the covariance matrix computed between the signal vectors of two different subarrays as their cross-covariance matrix. Each subarray then transmits its estimated self-covariance matrix and one-bit version of the measured data to the processing center. Transmitting only the one-bit data significantly reduces communication traffic compared to transmitting the full-precision raw data. The processing center computes the cross-covariance matrices between subarray pairs using the one-bit data. These one-bit cross-covariance matrices and the full-precision subarray self-covariance matrices computed by the subarrays are combined to form the full-array covariance matrix.

Recently, one-bit data processing has received extensive interest in the field of array signal processing, for example, in DOA estimation and (MIMO) processing problems [25–31]. However, relying only on one-bit data degrades the DOA estimation performance. The proposed approach avoids this performance degradation by using full-precision self-covariance matrices for all subarrays, which have a small size for transmission to the processing center. This keeps the communication traffic low.

The computed full-array covariance matrix is associated with sparse sensor placement due to the sparse subarray configurations as well as the dis-

placement between the subarrays. Therefore, the resulting DOA estimation performance suffers from high sidelobes. Assuming a moderate level of sensor sparsity, we use matrix completion methods to interpolate the missing holes in a half-wavelength grid so that the DOFs can be increased and the sidelobe effects in the estimated spatial spectrum can be minimized [32–40]. Considering that the spacing between the subarrays may not be an integer multiple of half-wavelength, an iterative DOA estimation method is proposed that compensates for the phase shift due to off-grid displacement. After the covariance matrix is fully interpolated, we use the MUSIC algorithm [41] to perform gridless DOA estimation. To provide an insightful understanding of the offerings of the proposed approach, a pessimistic Cramér-Rao bound (CRB) is also provided.

The offerings of this paper are summarized below:

1. A low-complexity collaborative DOA estimation scheme is proposed that utilizes full-precision data for local self-covariance matrix computation and one-bit data for cross-covariance matrix computation.

2. We apply a covariance matrix interpolation scheme to perform DOA estimation that accounts for off-grid subarray alignments.

3. An iterative DOA estimation approach is developed to compensate for the off-grid subarray displacement and provide improved estimation of the cross-covariance matrices for the off-grid subarray displacement scenario.

4. We provide a pessimistic CRB analysis to understand the importance of full-precision self-covariance matrix and the inclusion of cross-covariance, as well as the effect of data precision on cross-covariance matrix computation.

The idea of utilizing one-bit cross-covariance matrices was first presented in [1], and the CRB was analyzed in [2]. In [1], identical uniform linear arrays (ULAs) are used in the subarrays, and all sensors are assumed to be aligned to the half-wavelength grid. In contrast, this paper assumes sparse arrays in the subarrays, and the sparse array configurations may differ, and sensor interpolation is considered. The consideration for off-grid subarray placement is completely new, and an iterative method is developed to account for the unknown phase due to off-grid subarray placement. We further added

4

a comparison of the required data bits and revealed the superiority of the proposed method over full-precision and one-bit data cases in traffic-limited networks.

It is noted that there are recent reports on employing mixed-resolution analog-to-digital converters (ADCs) in massive MIMO systems to reduce the processing complexity and power consumption with a low performance loss [42–44]. For example, in [42], a nested array is considered where low-resolution ADCs are used for the inner subarray and high-resolution ADCs are used for the outer subarray. In [44], DOA estimation for coprime MIMO radar is considered, where the array antennas are grouped into low-resolution and high-resolution subsets. Furthermore, the authors in [45] proposed a method that can identify more targets and achieve better performance than existing subspace-based algorithms while deriving the CRB for nested MIMO radars. In [43], mixed-ADCs are used in massive MIMO systems with hybrid analog and digital beamformers. Because these applications consider collocated antennas, such systems do not involve network traffic, so both the signal model and processing approaches differ from our problem. Unlike our problem, where the self-covariance matrices are accurate and the data precision is only compromised in the cross-covariance matrices, the resolution in a massive MIMO system is limited by the ADCs, and such resolution is shared in the computation of all correlations.

The remainder of the paper is organized as follows. In Section 2, we formulate the signal model of the proposed collaborative DOA estimation scheme and describe the subarray self-covariance matrices computed locally at each subarray and the cross-covariance matrices between different pairs of subarrays computed at the processing center. Section 3 describes the covariance matrix interpolation using structured matrix completion techniques and performs DOA estimation when all subarrays are aligned to the half-wavelength grid. Covariance matrix interpolation and DOA estimation involving subarrays in off-grid positions are considered in Section 4, where an iterative DOA estimation approach is proposed. In Section 5, we analyze the pessimistic CRB of the underlying DOA estimation problem. In Section 6, we numerically evaluate the DOA estimation performance of the proposed scheme, and the results are compared to different situations where the cross-covariance matrices are estimated with full-precision data or are based only on one-bit data. It is learned that the performance of the proposed technique is slightly inferior to the case where the covariance matrices are provided with full precision but is significantly better than the case when cross-covariance

5

matrices are unavailable. Matrix completion exploiting the Toeplitz and Hermitian properties of the covariance matrix also assumes that all sensors are on a half-wavelength grid. Situations that violate these assumptions will be considered in separate works.

Notations: Lower-case and upper-case bold characters are used to represent vectors and matrices, respectively. In particular, $\mathbf{I}_N$ denotes the identity matrix of dimension $N \times N$, $\mathbf{1}$ denotes a vector or a matrix with all elements to be unity, and $\mathbf{0}$ denotes a vector or matrix with all elements to be zero. $(.)^{\mathrm{T}}$, $(.)^*$, and $(.)^{\mathrm{H}}$ stand for the transpose, conjugate, and conjugate transpose (Hermitian) operations, respectively. and $(\cdot)^{\dagger}$ denotes the Moore-Penrose inversion of a matrix. $\| \cdot \|_{\mathrm{F}}$ denotes the Frobenius norm, $\circ$, $\odot$, and $\otimes$ respectively denote the Hadamard, Khatri-Rao, and Kronecker products, and $\mathbf{A} \succeq 0$ implies that matrix $\mathbf{A}$ is positive semidefinite. In addition, $\mathrm{vec}(\cdot)$ and $\mathrm{tr}(\cdot)$ respectively perform the vectorization and trace operations on a matrix, and $\mathcal{T}(\boldsymbol{z})$ represents a Hermitian and Toeplitz matrix that takes vector $\boldsymbol{z}$ as its first column. $\mathrm{diag}(\cdot)$ and $\mathrm{bdiag}(\cdot)$ respectively form diagonal and block diagonal matrices. In addition, $[\mathbf{A}]_{p,q}$ denotes the (p,q)th element of matrix $\mathbf{A}$, whereas $\langle \mathbf{v} \rangle_i$ denotes the ith entry of vector $\mathbf{v}$. $\mathbb{E}[\cdot]$ performs statistical expectation, and $\mathcal{Q}(\cdot)$ denotes the element-wise one-bit quantization operation. $\jmath$ is used to denote the unit imaginary number, and $\mathcal{R}(\cdot)$ and $\mathcal{I}(\cdot)$ respectively return the real and imaginary parts of a complex number. We use $\mathbb{C}^{M \times N}$ to denote the $M \times N$ complex space, and $\mathbb{Z}^+$ stands for the set of positive integers.

2. System Model

Consider a collaborative array platform consisting of K collocated subarrays. The locations of the M_k sensors of the kth subarray are given as

$$\mathbb{S}_k = \{p_{k,1}d, p_{k,2}d, \ldots, p_{k,M_k}d\}, \tag{1}$$

where $k = 1, \ldots, K$, $d = \lambda/2$, and λ is the signal wavelength. The first sensor of the first subarray is set as the reference of the entire array, i.e., $p_{1,1} = 0$. For each subarray, the first sensor of the subarray serves as a local reference.

We assume that all subarray locations are synchronized and their sensor locations, $\mathbb{S}_1, \cdots, \mathbb{S}_K$, are known. In addition, in each subarray, the sensor positions $p_{k,m}d$ relative to their respective reference sensor position $p_{k,1}d$ are considered integer multiples of d, i.e., $(p_{k,m} - p_{k,1}) \in \mathbb{Z}^+ \ \forall k, m$. However, the displacement between the reference sensor of a subarray, $p_{k,1}d$ is

6

not necessarily an integer multiple of d for $k \geq 2$. From practicality of the subarray placement and for notation convenience without generality, we assume $p_{k_2,1} > p_{k_1,1}$ for any pair of subarrays with $k_2 > k_1$ and $p_{k+1,1} > p_{k,M_k}$ for $k = 1, \cdots, K-1$. This assumption ensures that $\mathbb{S}_{k_1} \cap \mathbb{S}_{k_2} = \emptyset$ for all $k_1 \neq k_2$ so that the full set of all array sensor is given as $\mathbb{S} = \bigcup_{k=1}^{K} \mathbb{S}_k$ without redundant elements in the resulting set.

When L uncorrelated far-field narrowband signals are received at the array from distinct directions $\boldsymbol{\theta} = [\theta_1, \cdots, \theta_L]^{\mathrm{T}}$, the baseband form of the signal vector received at the kth sparse subarray is expressed as:

$$\mathbf{x}_k(t) = \sum_{l=1}^{L} \mathbf{a}_k(\theta_l)s_l(t) + \mathbf{n}_k(t) = \mathbf{A}_k\mathbf{s}(t) + \mathbf{n}_k(t), \tag{2}$$

where $s_l(t)$ and θ_l denote the waveform and direction of the lth signal, respectively, $\mathbf{s}(t) = [s_1(t), \cdots, s_L(t)]^{\mathrm{T}}$, and

$$\mathbf{a}_k(\theta_l) = [e^{-\jmath p_{k,1}\pi \sin(\theta_l)}, e^{-\jmath p_{k,2}\pi \sin(\theta_l)}, \ldots e^{-\jmath p_{k,M_k}\pi \sin(\theta_l)}]^{\mathrm{T}} \tag{3}$$

is the steering vector of the kth subarray corresponding to the signal associated with direction θ_l. In addition, $\mathbf{n}_k(t)$ is the additive circularly complex white Gaussian noise vector observed at the kth subarray with mean $\mathbf{0}$ and covariance matrix $\sigma_{\mathrm{n}}^2\mathbf{I}_{M_k}$. We refer to $\mathbf{A}_k = [\mathbf{a}_k(\theta_1), \mathbf{a}_k(\theta_2), \ldots, \mathbf{a}_k(\theta_L)]$ as the manifold matrix of the kth subarray, and $\mathbf{A} = [\mathbf{A}_1^{\mathrm{T}}, \mathbf{A}_2^{\mathrm{T}}, \cdots \mathbf{A}_K^{\mathrm{T}}]^{\mathrm{T}}$ is defined as the manifold matrix of the entire array. It is noted that, because all signal and noise components are zero-mean, we use the terms correlation and covariance interchangeably.

Stacking the received signal vectors of all subarrays becomes

$$\mathbf{x}(t) = [\mathbf{x}_1^{\mathrm{T}}(t), \cdots, \mathbf{x}_K^{\mathrm{T}}(t)]^{\mathrm{T}} \in \mathbb{C}^{M \times 1}, \tag{4}$$

where $M = \sum_{k=1}^{K} M_k$ denotes the total number of sensors in the entire array.

2.1. Local Processing at Each Subarray

The self-covariance matrix of the data received at the kth subarray is expressed as:

$$\mathbf{R}_k = \mathbb{E}[\mathbf{x}_k(t)\mathbf{x}_k^{\mathrm{H}}(t)] = \mathbf{A}_k\mathbf{S}\mathbf{A}_k^{\mathrm{H}} + \sigma_{\mathrm{n}}^2\mathbf{I}_{M_k}$$
$$= \sum_{l=1}^{L} \sigma_l^2\mathbf{a}_k(\theta_l)\mathbf{a}_k^{\mathrm{H}}(\theta_l) + \sigma_{\mathrm{n}}^2\mathbf{I}_{M_k}, \tag{5}$$

where σ_l^2 denotes the power of the lth signal for $l = 1, \ldots, L$ and $\mathbf{S} = \mathbb{E}[\mathbf{s}(t)\mathbf{s}^{\mathrm{H}}(t)] = \mathrm{diag}([\sigma_1^2, \sigma_2^2, \cdots, \sigma_L^2])$ is the diagonal source covariance matrix.

In practice, the self-covariance matrix of each subarray is estimated using T available data samples, i.e.,

$$\hat{\mathbf{R}}_k = \frac{1}{T} \sum_{t=1}^{T} \mathbf{x}_k(t)\mathbf{x}_k^{\mathrm{H}}(t). \tag{6}$$

It is noted that, because $\hat{\mathbf{R}}_k$ is Hermitian and thus generally contain redundant entries associated with the same lags, only the unique entries of $\hat{\mathbf{R}}_k$ need to be transferred to the processing center.

In addition to $\hat{\mathbf{R}}_k$, the kth subarray quantizes the received data and sends the resulting one-bit complex data to the processing center. The real and imaginary parts of signal vector $\mathbf{x}_k(t)$ are respectively quantized, and the one-bit complex signal vector is expressed as [25]

$$\mathbf{y}_k(t) = \mathcal{Q}[\mathcal{R}(\mathbf{x}_k(t))] + \jmath\mathcal{Q}[\mathcal{I}(\mathbf{x}_k(t))]. \tag{7}$$

2.2. Centralized Processing at the Processing Center

The full-precision data cross-covariance matrix between the k_1th and k_2th subarrays is given as:

$$\begin{aligned}
\mathbf{R}_{k_1 k_2} &= \mathbb{E}[\mathbf{x}_{k_1}(t)\mathbf{x}_{k_2}^{\mathrm{H}}(t)] \\
&= \mathbf{A}_{k_1}\mathbf{S}\mathbf{A}_{k_2}^{\mathrm{H}} = \sum_{l=1}^{L} \sigma_l^2 \mathbf{a}_{k_1}(\theta_l)\mathbf{a}_{k_2}^{\mathrm{H}}(\theta_l).
\end{aligned} \tag{8}$$

The quantized one-bit cross-covariance matrix corresponding to $\mathbf{R}_{k_1 k_2}$ is expressed as

$$\begin{aligned}
\mathbf{R}_{k_1 k_2}^{[1\mathrm{B}]} &= \mathbb{E}[\mathbf{y}_{k_1}(t)\mathbf{y}_{k_2}^{\mathrm{H}}(t)] \\
&= \mathbf{A}_{k_1}\bar{\mathbf{S}}\mathbf{A}_{k_2}^{\mathrm{H}} = \sum_{l=1}^{L} \bar{\sigma}_l^2 \mathbf{a}_{k_1}(\theta_l)\mathbf{a}_{k_2}^{\mathrm{H}}(\theta_l),
\end{aligned} \tag{9}$$

where $\bar{\sigma}_l^2 = \sigma_l^2/(\sum_{l=1}^{L} \sigma_l^2 + \sigma_n^2)$ denotes the normalized power of the lth source for $l = 1, \ldots, L$, $k_1, k_2 = 1, \ldots, K$ with $k_1 \neq k_2$, and $\bar{\mathbf{S}} = \mathrm{diag}([\bar{\sigma}_1^2, \bar{\sigma}_2^2, \cdots, \bar{\sigma}_L^2])$ represents the normalized source covariance matrix [46].

If all K subarrays send the T_1 samples of full-precision raw data to the processing center, the processing center estimates the cross-covariance matrix

as

$$\hat{\mathbf{R}}_{k_1 k_2} = \frac{1}{T_1} \sum_{t=1}^{T} \mathbf{x}_{k_1}(t) \mathbf{x}_{k_2}^{\mathrm{H}}(t). \tag{10}$$

On the other hand, when the subarrays only send T_2 samples of the one-bit quantized data to the processing center, the processing center estimates the one-bit cross-covariance matrix between the k_1th and k_2th subarrays as

$$\hat{\mathbf{R}}_{k_1 k_2}^{[\mathrm{1B}]} = \frac{1}{T_2} \sum_{t=1}^{T} \mathbf{y}_{k_1}(t) \mathbf{y}_{k_2}^{\mathrm{H}}(t), \tag{11}$$

where superscript [1B] emphasizes that the results are obtained from one-bit quantized data.

For an arbitrary zero-mean stationary signal $z(t)$, the self-covariance $R_Z(\tau)$ between $z(t)$ and $z(t+\tau)$ is related to the one-bit counterpart $R_Z^{[\mathrm{1B}]}(\tau)$ by an arcsine relationship as [47, 48]

$$R_z^{[\mathrm{1B}]}(\tau) = \frac{2}{\pi} \sin^{-1} \left(\frac{R_z(\tau)}{R_z(0)} \right). \tag{12}$$

Note here that the self-covariance function $R_z(\tau)$ is normalized by $R_z(0)$ in the above computation because one-bit quantization results do not carry signal magnitude information. Similarly, the cross-covariance between $z_1(t)$ and $z_2(t + \tau)$ is obtained as

$$R_{z_1 z_2}^{[\mathrm{1B}]}(\tau) = \frac{2}{\pi} \sin^{-1} \left(\frac{R_{z_1 z_2}(\tau)}{\sqrt{R_{z_1}(0) R_{z_2}(0)}} \right). \tag{13}$$

As a result, by denoting

$$\bar{\mathbf{R}}_{k_1 k_2} = \sin\left(\frac{\pi}{2} \mathcal{R} \left[\hat{\mathbf{R}}_{k_1 k_2}^{[\mathrm{1B}]} \right] \right) + \jmath \sin\left(\frac{\pi}{2} \mathcal{I} \left[\hat{\mathbf{R}}_{k_1 k_2}^{[\mathrm{1B}]} \right] \right), \tag{14}$$

the cross-covariance matrix $\hat{\mathbf{R}}_{k_1 k_2}$ between subarrays k_1 and k_2 with the correct entry magnitudes is obtained from $\hat{\mathbf{R}}_{k_1 k_2}^{[\mathrm{1B}]}$ as

$$\hat{\mathbf{R}}_{k_1 k_2} = \hat{\mathbf{G}}_1^{1/2} \bar{\mathbf{R}}_{k_1 k_2} \hat{\mathbf{G}}_2^{1/2}, \tag{15}$$

where $\hat{\mathbf{G}}_k = \hat{\mathbf{R}}_k \circ \mathbf{I}_{M_k}$ is a diagonal matrix representing the power of the signals received at the kth subarray sensors.

9

3. Covariance Matrix Interpolation and DOA Estimation

In this section, we consider the DOA estimation with and without covariance matrix interpolation. First, we consider in Section 3.1 the case where no interpolation is applied. Section 3.2 considers covariance matrix interpolation when all sensor nodes are aligned on a half-wavelength grid. When the inter-subarray spacing is not an integer multiple of half-wavelength, we need to compensate for the phase-offset component due to the off-grid subarray positions. DOA estimation in such a general scenario is addressed in Section 4.

3.1. DOA Estimation without Covariance Matrix Interpolation

We generate the estimated covariance matrix of the full array vector $\mathbf{x}$ of all M sensors at the processing center by fusing the estimated subarray self- and cross-covariance matrices as follows:

$$\hat{\mathbf{R}} = \begin{bmatrix} \hat{\mathbf{R}}_1 & \hat{\mathbf{R}}_{1,2} & \cdots & \hat{\mathbf{R}}_{1,K} \\ \hat{\mathbf{R}}_{2,1} & \hat{\mathbf{R}}_2 & \cdots & \hat{\mathbf{R}}_{2,K} \\ \vdots & \vdots & \ddots & \vdots \\ \hat{\mathbf{R}}_{K,1} & \hat{\mathbf{R}}_{K,2} & \cdots & \hat{\mathbf{R}}_K \end{bmatrix} \in \mathbb{C}^{M \times M}. \tag{16}$$

In this case, MUSIC can be directly applied. We perform eigen-decomposition of matrix $\hat{\mathbf{R}}$ as

$$\hat{\mathbf{R}} = \hat{\mathbf{U}}\hat{\boldsymbol{\Sigma}}\hat{\mathbf{U}}^{\mathrm{H}} = \hat{\mathbf{U}}_{\mathrm{s}}\hat{\boldsymbol{\Sigma}}_{\mathrm{s}}\hat{\mathbf{U}}_{\mathrm{s}}^{H} + \hat{\mathbf{U}}_{\mathrm{n}}\hat{\boldsymbol{\Sigma}}_{\mathrm{n}}\hat{\mathbf{U}}_{\mathrm{n}}^{\mathrm{H}}, \tag{17}$$

where $\hat{\mathbf{U}}_{\mathrm{s}}$ and $\hat{\mathbf{U}}_{\mathrm{n}}$ contain columns that respectively span the signal and noise subspaces, whereas $\hat{\boldsymbol{\Sigma}}_{\mathrm{s}}$ and $\hat{\boldsymbol{\Sigma}}_{\mathrm{n}}$ are diagonal matrices containing the corresponding eigenvalues. Also, denote the full-array steering vector as the cascade of all subarrays, i.e.,

$$\mathbf{a}(\theta) = [\mathbf{a}_1^{\mathrm{T}}(\theta),\ \mathbf{a}_2^{\mathrm{T}}(\theta),\ \cdots,\ \mathbf{a}_K^{\mathrm{T}}(\theta)]^{\mathrm{T}}. \tag{18}$$

Then, MUSIC finds the DOAs of the L sources as the highest peaks of the following pseudo-spectrum:

$$P(\theta) = \frac{1}{\mathbf{a}^{\mathrm{H}}(\theta)\hat{\mathbf{U}}_{\mathrm{n}}\hat{\mathbf{U}}_{\mathrm{n}}^{\mathrm{H}}\mathbf{a}(\theta)}. \tag{19}$$

In this case, the array resolve up to $M-1$ sources and the estimated spectrum may subject to high sidelobe effects due to missing entries.
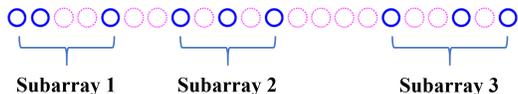
Figure 1: Sensor positions of the three lags.

3.2. Covariance Matrix Interpolation

Considering the distributed array with all sensors aligned on a half-wavelength grid with moderate separations, the problem is similar to the single-array interpolation problem considered in the literature [32–40], except that the cross-covariance matrices are obtained from one-bit data. We can use the same methods to interpolate a ULA to be interpolated with virtual sensor position at 0, 1, $\cdots$, $P = p_{K,M_K}$. In this paper, we use the method described in [37] due to its higher interpolation accuracy. A brief description of this approach is summarized below.

For the array configuration illustrated in Fig. 1, the self- and cross-covariance matrices are illustrated in Fig. 2(a). Black circles depict self-lags, whereas blue circles show cross-lags. Circles in magenta dash lines show missing entries.

The virtual signal vector of the difference coarray is obtained by vectorizing the covariance matrix $\hat{\mathbf{R}}$, given as

$$\hat{\mathbf{v}} = \text{vec}(\hat{\mathbf{R}}) = \mathbf{A}_v \mathbf{p} + \sigma_{\text{n}}^2 \mathbf{i}, \tag{20}$$

where $\mathbf{A}_v = \mathbf{A}^* \odot \mathbf{A}$, $\mathbf{p} = [\sigma_1^2, \sigma_2^2, \ldots, \sigma_K^2]^{\text{T}}$, and $\mathbf{i} = \text{vec}(\mathbf{I})$. Each element of $\hat{\mathbf{v}}$ corresponds to a virtual sensor. The positions of the virtual sensors are determined by the difference lags between the physical sensor positions. The entire set of virtual sensors obtained from the difference lags corresponding to all physical sensors is expressed as

$$\mathbb{D} = \{s_d | s_d = s_1 - s_2, s_1 \in \mathbb{S}, s_2 \in \mathbb{S}\}. \tag{21}$$

Because the self-covariance matrices that are locally computed at each subarray are more accurate than the cross-covariance matrices that are computed using one-bit data, it is reasonable to distinguish difference lags computed from self- and cross-covariance entries in the formed mixed-precision covariance matrix, particularly when both of them are available for some lags. That is, when a covariance corresponding to a specific lag (such as lag 5 and -5 in Fig. 2) is available for both self- and cross-covariance entries, we will use the self-covariance results because they have a higher accuracy.

11
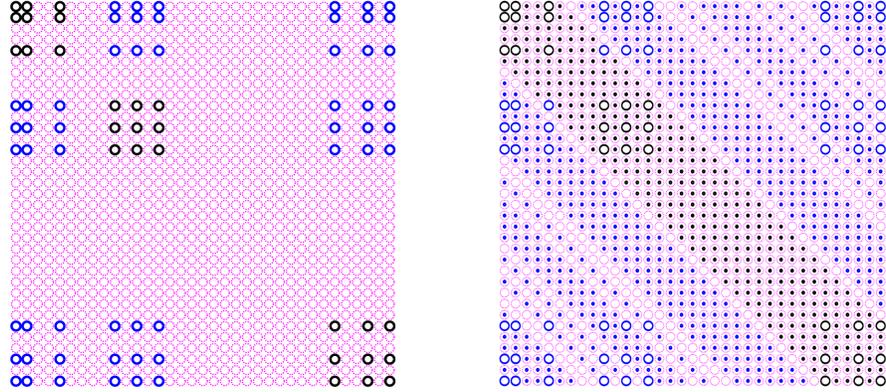
(a) Self- and cross-covariance matrix entries.

(b) Covariance matrix entries after filling with known lags.

Figure 2: Array covariance matrix before and after filling with known lag values (black circle: self-lags; blue circle: cross-lags; magenta circle: missing holes; black dot: filled with self-lags; blue dot: filled with cross-lags).

We define the lags generated from the self-covariance of the kth subarray as

$$\mathbb{D}_k^{[\text{self}]} = \left\{ s_d | s_d = s_1 - s_2, s_1 \in \mathbb{S}_k, s_2 \in \mathbb{S}_k \right\}. \tag{22}$$

The collection of all subarray self-lags constitutes the entire self-lag set, expressed as

$$\mathbb{D}^{[\text{self}]} = \left\{ \mathbb{D}_1^{[\text{self}]}, \ \mathbb{D}_2^{[\text{self}]}, \ \cdots, \mathbb{D}_K^{[\text{self}]} \right\}. \tag{23}$$

Note that some entries of $\mathbb{D}_1^{[\text{self}]}$, $\mathbb{D}_2^{[\text{self}]}$, $\cdots$, $\mathbb{D}_K^{[\text{self}]}$ may be redundant. The cross-lags are obtained as

$$\mathbb{D}^{[\text{cross}]} = \mathbb{D} \backslash \mathbb{D}^{[\text{self}]}, \tag{24}$$

where $\backslash$ denotes the difference between two sets. With such lags obtained, we can fill in the covariance matrix by utilizing the Toeplitz structure of the ULA spanning the entire array aperture. The covariance entries corresponding to the example shown in Fig. 2(a) are illustrated in Fig. 2(b), where missing entries filled by self-lags are depicted by black dots, whereas those filled with cross-lags are depicted by blue dots. As the result, most of the holes are filled, whereas the remaining holes will be filled using a matrix completion method.

We first initialize the ith element of the interpolated virtual array signal vector $\mathbf{v}_{\mathrm{I}} \in \mathbb{C}^{(2P+1)\times 1}$ as

$$\langle \mathbf{v}_{\mathrm{I}} \rangle_i = \begin{cases} \langle \hat{\mathbf{v}} \rangle_i, & i \in \mathbb{D}, \\ 0, & i \in \mathbb{S}_{\mathrm{I}} \backslash \mathbb{D}, \end{cases} \tag{25}$$

for $-P \leq i \leq P$, where $\mathbb{S}_{\mathrm{I}}$ denotes all virtual ULA positions between $-P$ and P. By dividing $\mathbf{v}_{\mathrm{I}}$ into $U = P + 1$ overlapping subvectors $\mathbf{r}_1, \mathbf{r}_2, \ldots$, and $\mathbf{r}_U$, we form matrix $\mathbf{V} = [\mathbf{r}_1, \ldots, \mathbf{r}_U] \in \mathbb{C}^{U \times U}$ which is Hermitian and Toeplitz.

Denote $\mathbf{g}(\theta)$ as the $U \times 1$ steering vector. Then, an atom that represents matrix $\mathbf{V}$ can be expressed as $\mathbf{G}(\theta) = \mathbf{g}(\theta)\mathbf{b}^{\mathrm{H}}(\theta) \in \mathbb{C}^{U \times U}$ for $\theta \in [-90°, 90°]$, where

$$\mathbf{b}(\theta) = [1, e^{-\jmath \pi \sin \theta}, \ldots, e^{-\jmath \pi (U-1) \sin \theta}]^{\mathrm{T}} \tag{26}$$

describes the relative phase offsets of the U columns of matrix $\mathbf{V}$ with respect to its first column [35, 37].

Letting

$$\mathbb{A} = \{\mathbf{G}(\theta) \mid \theta \in [-90°, 90°]\} \tag{27}$$

denote the full atom set, the smallest number of atoms that represent the virtual measurement matrix $\mathbf{V}$ is defined as

$$||\mathbf{V}||_{\mathbb{A},0} = \inf_K \left\{ \mathbf{V} = \sum_{k=1}^{K} p_k \mathbf{G}(\theta_k), p_k \geq 0 \right\}. \tag{28}$$

It is shown in [37] that problem (28) is equivalent to the following rank minimization problem:

$$\min_{\mathbf{z}, \mathbf{M}} \quad \mathrm{rank}[\mathcal{T}(\mathbf{z})]$$

$$\text{subject to} \quad \begin{bmatrix} \mathcal{T}(\mathbf{z}) & \mathbf{V} \\ \mathbf{V}^{\mathrm{H}} & \mathbf{M} \end{bmatrix} \succeq 0, \tag{29}$$

where $\mathbf{M}$ is a Hermitian and Toeplitz matrix. Let $\gamma > 0$ be a positive constant and $\mathbf{W} \succeq 0$ be a positive semidefinite matrix. Then, the above rank-minimization problem can be reformulated as [37, 38]:

$$\min_{\mathbf{z},\mathbf{W}} \quad \gamma^{-2}(\|\mathbf{W} - \gamma\mathbf{I}\|_F^2) + 2\mathrm{tr}[\mathbf{W}\mathcal{T}(\mathbf{z})]$$

$$\text{subject to} \quad \|\mathcal{T}(\mathbf{z}) \circ \mathbf{B} - \tilde{\mathbf{R}}_v\|_F \leq \eta,$$
$$\mathrm{tr}[\mathbf{W}\mathcal{T}(\mathbf{z})] \leq 0, \qquad\qquad (30)$$
$$\mathbf{W} \succeq 0,$$
$$\begin{bmatrix} \mathcal{T}(\mathbf{z}) & \mathbf{z} \\ \mathbf{z}^H & U^{-1}\mathrm{tr}[\mathcal{T}(\mathbf{z})] \end{bmatrix} \succeq 0,$$

where $\tilde{\mathbf{R}}_v = \mathcal{T}(\mathbf{r}_1)$ and $\mathbf{B} \in \mathbb{C}^{U \times U}$ is a binary matrix whose non-zero entries indicate derived statistics in $\tilde{\mathbf{R}}_v$, whereas zero values indicate interpolated results.

Once the covariance matrix of the ULA is estimated as $\mathcal{T}(\mathbf{z})$ from the above optimization problem, MUSIC algorithm is applied to perform gridless DOA estimation.

4. Iterative Method for DOA Estimation

In the previous sections, we assumed that all subarrays are on-grid, meaning that their positions are defined by integer multiples of a half-wavelength. In practice, we can align all sensors within a subarray, but we usually do not have full control over the subarray positions. In other words, while subarray sensors may be spaced an integer multiple of a half-wavelength apart, the subarrays themselves, represented by the reference sensor position of each subarray, may not be exactly aligned with the on-grid positions. Motivated by this fact, in this section, we develop a new iterative DOA estimation technique which enables application to such scenarios with off-grid subarray positions and provides improved DOA estimation performance.

Consider that the reference sensor of the kth subarray is located at position $\tilde{p}_{k,1}d = p_{k,1}d + \epsilon_k$, where $\tilde{p}_{k,1}$ is generally a non-integer, $p_{k,1}d$ is the closest integer to $\tilde{p}_{k,1}$ indicating an on-grid position, and ϵ_k with $|\epsilon_k| \leq d/2 = \lambda/4$ is the fraction part of the reference sensor position of the kth subarray with respect to half-wavelength. It is assumed that the off-grid displacement of all subarrays, $\tilde{p}_{k,1}$, $k = 2, \cdots, K$, is known.

Considering the off-grid subarray positions, the steering vector of the kth

14

subarray is expressed as

$$\tilde{\mathbf{a}}_k(\theta) = \left[e^{-\jmath \tilde{p}_{k,1} \pi \sin(\theta)}, e^{-\jmath \tilde{p}_{k,2} \pi \sin(\theta)}, \cdots, e^{-\jmath \tilde{p}_{k,M_k} \pi \sin(\theta)} \right]^{\mathrm{T}}$$
$$= \exp(-\jmath 2\pi \epsilon_k \sin(\theta)) \mathbf{a}_k(\theta), \tag{31}$$

where $\mathbf{a}_k(\theta)$ is given in (3) and is computed based on the nearest on-grid sensor position. In this case, the data received by the kth subarray becomes

$$\mathbf{x}_k(t) = \tilde{\mathbf{A}}_k \mathbf{s}(t) + \mathbf{n}_k(t) = \mathbf{A}_k \mathbf{\Phi}_k \mathbf{s}(t) + \mathbf{n}_k(t), \tag{32}$$

where $\tilde{\mathbf{A}}_k = \mathbf{A}_k \mathbf{\Phi}_k$ and $\mathbf{A}_k$ are respectively the array manifold matrices corresponding to $\tilde{\mathbf{a}}_k(\theta)$ and $\mathbf{a}_k(\theta)$. As such, the matrix

$$\mathbf{\Phi}_k = \mathrm{diag}\left([\exp(-\jmath 2\pi \epsilon_k \sin(\theta_1)), \cdots, \exp(-\jmath 2\pi \epsilon_k \sin(\theta_L))] \right) \tag{33}$$

relating these two matrices represents the phase-offset due to the off-grid subarray positions. It is clear that such off-grid subarray position issue only affects the cross-covariance matrices between subarrays which, for subarrays k_1 and k_2, now become

$$\mathbf{R}_{k_1 k_2}^{[\mathrm{1B}]} = \mathbb{E}[\mathbf{y}_{k_1}(t) \mathbf{y}_{k_2}^{\mathrm{H}}(t)] = \tilde{\mathbf{A}}_{k_1} \bar{\mathbf{S}} \tilde{\mathbf{A}}_{k_2}^{\mathrm{H}} = \mathbf{A}_{k_1} \mathbf{\Phi}_{k_1 k_2} \bar{\mathbf{S}} \mathbf{A}_{k_2}^{\mathrm{H}}, \tag{34}$$

which depends on $\mathbf{\Phi}_{k_1 k_2} = \mathbf{\Phi}_{k_1} \mathbf{\Phi}_{k_2}^{\mathrm{H}}$, whereas the self-covariance matrix of each subarray, given in (5), is unaffected because $\mathbf{\Phi}_{kk} = \mathbf{I}_{M_k}$ for all k.

Based on the estimates of $\mathbf{R}_{k_1 k_2}^{[\mathrm{1B}]}$ and $\mathbf{R}_k$, we can obtain the estimated full-array covariance matrix $\hat{\mathbf{R}}$ in (16) as the input to initiate the iterative DOA estimation approach described below.

The total covariance matrix $\hat{\mathbf{R}}$ is interpolated and the DOAs of the L sources are estimated. Let the estimated DOAs of the sources obtained in the ith iteration be denoted as $\hat{\boldsymbol{\theta}}^{(i)} = [\hat{\theta}_1^{(i)}, \cdots, \hat{\theta}_L^{(i)}]^{\mathrm{T}}$. Based on these estimated DOAs at the ith iteration, we compute the steering vector for the off-grid position case using (31), and the corresponding array manifold of the individual subarrays as $\tilde{\mathbf{A}}_k^{(i+1)} = [\tilde{\mathbf{a}}_k(\hat{\theta}_1^{(i)}), \tilde{\mathbf{a}}_k(\hat{\theta}_2^{(i)}), \cdots, \tilde{\mathbf{a}}_k(\hat{\theta}_L^{(i)})]$ for $k = 1, \cdots, K$. Furthermore, the power of the lth source in the ith iteration is estimated as [51]

$$(\hat{\sigma}_l^2)^{(i)} = \frac{1}{(\tilde{\mathbf{a}}(\hat{\theta}_l^{(i)}))^{\mathrm{H}} \hat{\mathbf{U}}_s (\hat{\mathbf{\Sigma}}_s)^{-1} (\hat{\mathbf{U}}_s)^{\mathrm{H}} \tilde{\mathbf{a}}(\hat{\theta}_l^{(i)})}, \tag{35}$$

15

where $\hat{\mathbf{U}}_s$ denotes the signal subspace corresponding to the interpolated covariance matrix $\hat{\mathbf{R}}$ obtained by using (34) and (10), and $\hat{\boldsymbol{\Sigma}}_{\mathbf{s}}$ denotes the diagonal matrix of the corresponding eigenvalues. The use of the signal subspace in the matrix inversion provides more accurate estimation of the signal power as compared to the commonly used total covariance matrix inversion, particularly when the input signal-to-noise ratio (SNR) is low [51].

Based on the estimated signal DOAs and power of all the L sources, we can estimate the source covariance matrix $\hat{\mathbf{S}}^{(i)} = \mathrm{diag}([(\hat{\sigma}_1^2)^{(i)}, (\hat{\sigma}_2^2)^{(i)}, \cdots, (\hat{\sigma}_L^2)^{(i)}])$. Denote $\hat{\mathbf{x}}_k^{(i)}(t) = \tilde{\mathbf{A}}_k^{(i)}\mathbf{s} + \mathbf{n}_k(t)$ as the received array data corresponding to the array manifold $\tilde{\mathbf{A}}_k^{(i)}$ estimated at the ith iteration, the estimated cross-covariance matrix between subarrays k_1 and k_2 in the ith iteration can be obtained as

$$\tilde{\mathbf{R}}_{k_1 k_2}^{(i)} = \mathbb{E}\left[\hat{\mathbf{x}}_{k_1}^{(i)}(t)\left(\hat{\mathbf{x}}_{k_2}^{(i)}(t)\right)^{\mathrm{H}}\right] = \hat{\mathbf{A}}_{k_1}^{(i)}\hat{\mathbf{S}}^{(i)}\left(\hat{\mathbf{A}}_{k_2}^{(i)}\right)^{\mathrm{H}}. \tag{36}$$

Once the cross-covariance matrices between all subarray pairs are computed with the phase-offset terms compensated at the end of the iterative steps, the corresponding cross-covariance matrices in (16) are replaced by that obtained from (36), which is then interpolated following the method developed in [37] to form the interpolated covariance matrix. In this matrix, the effect of the off-grid subarray displacement is nullified, and thus the precision of the estimation is improved. The DOA estimation is performed on the interpolated covariance matrix by employing subspace-based approaches, such as MUSIC, as discussed in the previous section. The iteration is continued until the stopping criterion is met. Such stopping criterion typically includes that a predetermined number of iterations $N_{\max}$ is executed, or the desired estimation accuracy is achieved, e.g., $\max_l |\hat{\theta}_l^{(i)} - \hat{\theta}_l^{(i-1)}| \leq \epsilon_\theta$, where ϵ_θ is a predefined bound. The proposed iterative method is summarized in Algorithm 1.

The computational complexity of our proposed method is separately considered for the DOA estimation when all subarrays are aligned to the half-wavelength grid, and the additional iterative approach to compensate for the off-grid subarray displacements. For the former, the complexity of the proposed algorithm is primarily dominated by the matrix completion required to interpolate the covariance matrix $\hat{\mathbf{R}}^{(i)}$, which is described in Section 3.2 with a complexity of $\mathcal{O}(M^4)$ [38], and the eigen-decomposition of the completed covariance matrix required to perform the MUSIC algorithm, whose

16

complexity is given as $\mathcal{O}(M^3)$ [49, 50]. As such, the overall complexity is denoted as $\mathcal{O}(M^4)$.

The iterative approach closely follows the similar steps in each iteration, including matrix completion and DOA estimation, with an additional step of signal power estimation. Therefore, the computational complexity required to perform each iteration is $\mathcal{O}(M^4)$, and the total complexity of the iterative algorithm is $N_{\max} \cdot \mathcal{O}(M^4)$.

When simulations are carried out for the distributed array depicted in Fig. 1 and reported in Section 6 using an Intel(R) Core(TM) i7-1065G7 CPU with 16 GB memory, the initial DOA estimation phase takes 2.5 seconds, whereas the time needed to perform 2 iterations of the iterative subarray displacement compensation is 4.8 seconds.

Algorithm 1 Proposed Iterative DOA Estimation Method

Input: $\{\mathbf{y}_k(t)\}_{k=1}^K$, $\{\hat{\mathbf{R}}_k\}_{k=1}^K$, $\{\tilde{p}_{k,1}\}_{k=1}^K$, $N_{\max}$, ϵ_θ
Output: $\{\hat{\theta}_l\}_{l=1}^L$

1: Compute $\{\hat{\mathbf{R}}_{k_1 k_2}^{[1\mathrm{B}]}\}_{k_1,k_2=1}^K$ from (11)
2: Construct $\hat{\mathbf{R}}$ in (16) using all $\hat{\mathbf{R}}_k$ and $\hat{\mathbf{R}}_{k_1 k_2}^{[1\mathrm{B}]}$
3: Interpolate $\hat{\mathbf{R}}$ using (30)
4: Estimate the DOAs $\{\hat{\theta}_l^{(0)}\}_{l=1}^L$ by applying MUSIC to $\hat{\mathbf{R}}$
5: **for** $i = 1 : N_{\max}$ **do**
6:      Estimate $\tilde{\mathbf{a}}(\hat{\theta}_l^{(i)})$ from (31) and $(\hat{\sigma}_l^2)^{(i)}$ from (35) using $\{\hat{\theta}_l^{(i-1)}\}_{l=1}^L$
7:      Construct $\hat{\mathbf{S}}^{(i)}$ using estimated source powers
8:      Update $\{\mathbf{R}_{k_1 k_2}^{[1\mathrm{B}]}\}_{k_1,k_2=1}^K$ using (36)
9:      Update $\hat{\mathbf{R}}^{(i)}$ using (16)
10:      Estimate the DOAs $\{\hat{\theta}_l^{(i)}\}_{l=1}^L$ by applying MUSIC to $\hat{\mathbf{R}}^{(i)}$
11:      **if** $\max_l |\hat{\theta}_l^{(i)} - \hat{\theta}_l^{(i-1)}| \le \epsilon_\theta$ **then**
12:         break
13:      **end if**
14: **end for**

---

5. CRB Analysis

To carry out the CRB analysis, we construct the parameter vector $\boldsymbol{\psi} = [\boldsymbol{\omega}^{\mathrm{T}}, \mathbf{p}^{\mathrm{T}}, \sigma_{\mathrm{n}}^2]^{\mathrm{T}}$, where the spatial frequencies and power of the L sources are

given as $\boldsymbol{\omega} = [\omega_1, \cdots, \omega_L]^{\mathrm{T}}$ and $\mathbf{p} = [\sigma_1^2, \sigma_2^2, \cdots, \sigma_L^2]^{\mathrm{T}}$, respectively. Note that the spatial frequency ω_l of the lth source is related to its DOA θ_l by $\omega_l = d \sin(\theta_l)/\lambda = \sin(\theta_l)/2$. Therefore, the cardinality of the unknown parameter vector is $2L + 1$.

The true probability density function (PDF) of one-bit data is obtained from the orthant probabilities [52] of Gaussian distribution which, in general, does not have a closed-form expression [46]. Instead, a pessimistic closed-form approximation is used in [46] to derive the CRB of the estimated DOAs obtained from one-bit sparse linear array data. The Gaussian assumption leads to the largest, i.e., most pessimistic, CRB results in a general class of data distributions [53].

5.1. Probability Model

Assuming uncorrelated incoming signals [54, 55], we determine the stochastic CRB by employing the pessimistic model as described in [46]. We utilize the previously mentioned relationship between covariances derived from full-precision data and those from one-bit data, and model $\mathbf{x}(t)$ to follow a complex Gaussian distribution with zero mean and covariance matrix $\mathbf{R}$, i.e., $\mathbf{x}(t) \sim \mathcal{CN}(\mathbf{0}, \mathbf{R})$, where

$$\mathbf{R} = \mathbb{E}[\mathbf{x}(t)\mathbf{x}^{\mathrm{H}}(t)]$$

$$= \begin{bmatrix} \mathbf{R}_1 & \mathbf{R}_{1,2} & \cdots & \mathbf{R}_{1,K} \\ \mathbf{R}_{2,1} & \mathbf{R}_2 & \cdots & \mathbf{R}_{2,K} \\ \vdots & \vdots & \ddots & \vdots \\ \mathbf{R}_{K,1} & \mathbf{R}_{K,2} & \cdots & \mathbf{R}_K \end{bmatrix}.$$

In this expression, the block diagonal elements denoted as $\mathbf{R}_k$ represents the self-covariance matrix for the kth subarray and is defined in (5), whereas $\mathbf{R}_{k_1,k_2}$ is the cross-covariance matrix between the k_1th and the k_2th subarrays obtained using the one-bit data, given as

$$\mathbf{R}_{k_1 k_2} = \mathbf{G}_1^{1/2} \bar{\mathbf{R}}_{k_1 k_2} \mathbf{G}_2^{1/2}, \tag{37}$$

and $\mathbf{G}_k = \mathbf{R}_k \circ \mathbf{I}_{M_k}$. In the above expression,

$$\bar{\mathbf{R}}_{k_1 k_2} = \sin\left(\frac{\pi}{2} \mathcal{R}\left[\mathbf{R}_{k_1 k_2}^{[1\mathrm{B}]}\right]\right) + \jmath \sin\left(\frac{\pi}{2} \mathcal{I}\left[\mathbf{R}_{k_1 k_2}^{[1\mathrm{B}]}\right]\right), \tag{38}$$

where $\mathbf{R}_{k_1 k_2}^{[1\mathrm{B}]}$ is defined in (9). It is noted that, because noise components observed at different sensors are uncorrelated, cross-covariance matrices do not include noise terms.

5.2. Formulation of the CRB

Consider a random vector $\mathbf{x}$ with a conditional PDF given as $p(\mathbf{x}|\psi)$, where ψ is a deterministic parameter vector. Denote ψ_p as the pth element of the unknown parameter vector $\boldsymbol{\psi}$. Then, for $p, q \in \{1, 2, \cdots, 2L + 1\}$, the general expression for the (p, q)th element of the Fisher information matrix (FIM) is given by

$$[\mathbf{F}]_{p,q} = -\mathbb{E}\left\{\frac{\partial^2 \ln p(\mathbf{x}|\boldsymbol{\psi})}{\partial \psi_p \partial \psi_q}\right\}. \tag{39}$$

When T samples are used in the estimation of the covariance entries, the formulation closely follows the existing results that are derived for sparse arrays [55]. In this case, denoting $\mathbf{r} = \text{vec}(\mathbf{R}) \in \mathbb{C}^{M^2 \times 1}$, (39) can be written as [55–57]:

$$
\begin{aligned}
[\mathbf{F}]_{p,q} &= T \cdot \text{tr}\left(\mathbf{R}^{-1}\frac{\partial \mathbf{R}}{\partial \psi_p}\mathbf{R}^{-1}\frac{\partial \mathbf{R}}{\partial \psi_q}\right) \\
&= T \cdot \left[\left(\mathbf{R}^{\mathrm{T}} \otimes \mathbf{R}\right)^{-1/2}\frac{\partial \mathbf{r}}{\partial \psi_p}\right]^{\mathrm{H}}\left[\left(\mathbf{R}^{\mathrm{T}} \otimes \mathbf{R}\right)^{-1/2}\frac{\partial \mathbf{r}}{\partial \psi_q}\right].
\end{aligned}
\tag{40}
$$

The parameters of interest for which we would like to find the CRB are spatial frequencies of the signals, i.e., $\boldsymbol{\omega}$. Thus, we divide the parameter vector as $\boldsymbol{\psi} = [\boldsymbol{\omega}^{\mathrm{T}} \ \ \mathbf{o}]^{\mathrm{T}}$, where $\mathbf{o} = [\mathbf{p}^{\mathrm{T}} \ \ \sigma_{\mathrm{n}}^2]$ consists of the signal and noise power terms. Then, the total FIM can be decomposed into components that are respectively associated with the spatial frequencies and other terms, given as

$$\mathbf{F} = T \cdot \begin{bmatrix}\boldsymbol{\Delta}_{\boldsymbol{\omega}} \\ \boldsymbol{\Delta}_{\mathbf{o}}\end{bmatrix}^{\mathrm{H}}[\boldsymbol{\Delta}_{\boldsymbol{\omega}} \ \ \boldsymbol{\Delta}_{\mathbf{o}}] = T \cdot \begin{bmatrix}\boldsymbol{\Delta}_{\boldsymbol{\omega}}^{\mathrm{H}}\boldsymbol{\Delta}_{\boldsymbol{\omega}} & \boldsymbol{\Delta}_{\boldsymbol{\omega}}^{\mathrm{H}}\boldsymbol{\Delta}_{\mathbf{o}} \\ \boldsymbol{\Delta}_{\mathbf{o}}^{\mathrm{H}}\boldsymbol{\Delta}_{\boldsymbol{\omega}} & \boldsymbol{\Delta}_{\mathbf{o}}^{\mathrm{H}}\boldsymbol{\Delta}_{\mathbf{o}}\end{bmatrix}, \tag{41}$$

where

$$\boldsymbol{\Delta}_{\boldsymbol{\omega}} = \left(\mathbf{R}^{T} \otimes \mathbf{R}\right)^{-\frac{1}{2}}\left[\frac{\partial \mathbf{r}}{\partial \omega_1}, \cdots, \frac{\partial \mathbf{r}}{\partial \omega_L}\right] \tag{42}$$

and

$$\boldsymbol{\Delta}_{\mathbf{o}} = \left(\mathbf{R}^{T} \otimes \mathbf{R}\right)^{-\frac{1}{2}}\left[\frac{\partial \mathbf{r}}{\partial \sigma_1^2}, \cdots, \frac{\partial \mathbf{r}}{\partial \sigma_L^2}, \frac{\partial \mathbf{r}}{\partial \sigma_{\mathrm{n}}^2}\right]. \tag{43}$$

When the FIM is nonsingular, following the derivation in [55], the CRB of $\boldsymbol{\omega}$ can be obtained as the inverse of the Schur complement of the $\boldsymbol{\Delta}_{\mathbf{o}}^{\mathrm{H}}\boldsymbol{\Delta}_{\mathbf{o}}$ block as [58]:

$$\text{CRB}(\boldsymbol{\omega}) = \frac{1}{T}(\boldsymbol{\Delta}_{\boldsymbol{\omega}}^{\mathrm{H}}\boldsymbol{\Pi}_{\mathbf{o}}^{\perp}\boldsymbol{\Delta}_{\boldsymbol{\omega}})^{-1}, \tag{44}$$

19

where $\mathbf{\Pi}_{\mathbf{o}}^{\perp} = \mathbf{I} - \mathbf{\Delta}_{\mathbf{o}}(\mathbf{\Delta}_{\mathbf{o}}^{\mathrm{H}}\mathbf{\Delta}_{\mathbf{o}})^{-1}\mathbf{\Delta}_{\mathbf{o}}^{\mathrm{H}}$ denotes the orthogonal projection onto the null space of $\mathbf{\Delta}_{\mathbf{o}}$.

In the following subsections, we formulate the FIM and CRB expressions for the full-precision and the one-bit data model for the distributed sparse arrays based on [55] and [46] respectively. The CRB analysis for the mixed-precision data model will then follow.

5.3. CRB and FIM for Full-Precision Data Model

Denote $\mathbb{D}$ as the lags resulting from the difference coarray of the entire array, and D as the number of non-negative elements in $\mathbb{D}$ such that $|\mathbb{D}| = 2D - 1$ [24]. Define $\mathbf{a}_{\mathbb{D}}(\theta_l) \in \mathbb{C}^{(2D-1)\times 1}$ as the steering vector of the difference coarray corresponding to the lth signal and $\mathbf{J} \in \{0,1\}^{M^2 \times (2D-1)}$ as a binary selection mask such that $\mathbf{a}^*(\theta_l) \otimes \mathbf{a}(\theta_l) = \mathbf{J}\mathbf{a}_{\mathbb{D}}(\theta_l)$. We obtain the covariance matrix from the full-precision data as $\mathbf{R}_{\mathrm{FP}}$, and its vectorized result is expressed as

$$\mathbf{r}_{\mathrm{FP}} = \sum_{l=1}^{L} \sigma_l^2 \mathbf{J}\mathbf{a}_{\mathbb{D}}(\theta_l) + \sigma_{\mathrm{n}}^2 \mathrm{vec}(\mathbf{I}_M). \tag{45}$$

We obtain the partial derivative of $\mathbf{r}_{\mathrm{FP}}$ corresponding to the spatial frequency of the lth signal, ω_l, as

$$\frac{\partial \mathbf{r}_{\mathrm{FP}}}{\partial \omega_l} = -\jmath 2\pi\sigma_l^2 \cdot \mathbf{J} \cdot \mathrm{diag}(\mathbb{D}) \cdot \mathbf{a}_{\mathbb{D}}(\theta_l), \tag{46}$$

whereas the partial derivatives of $\mathbf{r}_{\mathrm{FP}}$ with respect to the signal power σ_l^2 of the lth signal and to the noise power σ_{n}^2 are respectively given as

$$\frac{\partial \mathbf{r}_{\mathrm{FP}}}{\partial \sigma_l^2} = \mathbf{J}\mathbf{a}_{\mathbb{D}}(\theta_l) \tag{47}$$

and

$$\frac{\partial \mathbf{r}_{\mathrm{FP}}}{\partial \sigma_{\mathrm{n}}^2} = \mathrm{vec}(\mathbf{I}_M). \tag{48}$$

Therefore, when full-precision array data are used, substituting (46)–(48) into (41)–(44) yields the FIM and the CRB of the DOA estimates.

5.4. FIM and CRB for One-Bit Data Model

For the CRB and FIM expressions of the one-bit data model, we consider the entire array as a sparse linear array and compute the full-precision normalized cross-covariance matrix $\bar{\mathbf{R}}_{\text{FP}}$ as

$$\bar{\mathbf{R}}_{\text{FP}} = \mathbf{A}\text{diag}(\bar{\mathbf{p}})\mathbf{A}^{\text{H}} + \left(1 - \sum_{l=1}^{L} \bar{\sigma}_l^2\right) \mathbf{I}_M. \tag{49}$$

Utilizing the arcsine law, the corresponding covariance matrix obtained from the one-bit data is expressed as

$$\mathbf{R}_{\text{1B}} = \frac{2}{\pi}\text{arcsine}\left(\bar{\mathbf{R}}_{\text{FP}}\right). \tag{50}$$

Substituting (49) to (50) and vectorizing, we obtain

$$\mathbf{r}_{\text{1B}} = \frac{2}{\pi}\mathbf{J} \cdot \text{arcsine}\left[\mathbf{A}_{\mathbb{D}}\bar{\mathbf{p}} + \left(1 - \sum_{l=1}^{L} \bar{\sigma}_l^2\right)\mathbf{e}\right], \tag{51}$$

where $\mathbf{A}_{\mathbb{D}} = [\mathbf{a}_{\mathbb{D}}(\theta_1), \cdots, \mathbf{a}_{\mathbb{D}}(\theta_L)] \in \mathbb{C}^{(2D-1)\times L}$ and $\mathbf{e} \in \{0,1\}^{(2D-1)\times 1}$ is a column vector such that $\langle \mathbf{e}\rangle_D = 1$ and the other elements are zero.

The partial derivative of $\mathbf{r}_{\text{1B}}$ with respect to spatial frequency ω_l of the lth signal is formulated as

$$\frac{\partial \mathbf{r}_{\text{1B}}}{\partial \omega_l} = -4j\bar{\sigma}_l^2\mathbf{J} \cdot \text{diag}(\mathbb{D})\Big[\text{diag}(\bar{\mathbf{h}}) \cdot \mathcal{R}\left(\mathbf{a}_{\mathbb{D}}(\theta_l)\right) - \mathbf{e}$$
$$+ j\text{diag}(\mathbf{h}) \cdot \mathcal{I}\left(\mathbf{a}_{\mathbb{D}}(\theta_l)\right)\Big]. \tag{52}$$

Similarly, the partial derivatives of $\mathbf{r}_{\text{1B}}$ with respect to signal power σ_l^2 and the noise power σ_{n}^2 are respectively given as

$$\frac{\partial \mathbf{r}_{\text{1B}}}{\partial \sigma_l^2} = \frac{2}{\pi}\mathbf{J}\Big[\text{diag}(\mathbf{h}) \cdot \mathcal{R}\left(\mathbf{a}_{\mathbb{D}}(\theta_l)\right) - \mathbf{e}$$
$$+ j\text{diag}(\bar{\mathbf{h}}) \cdot \mathcal{I}\left(\mathbf{a}_{\mathbb{D}}(\theta_l)\right)\Big] \tag{53}$$

and

$$\frac{\partial \mathbf{r}_{\text{1B}}}{\partial \sigma_n^2} = \frac{2}{\pi}\mathbf{J}\left[\text{diag}(\mathbf{h}) \cdot \mathbf{e} + j\text{diag}(\bar{\mathbf{h}}) \cdot \mathbf{e}\right], \tag{54}$$

where $\mathbf{h} = [\mathrm{h}_{\mathbb{D}_1}, \cdots, \mathrm{h}_{\mathbb{D}_{2D-1}}]^{\mathrm{T}}$ and $\bar{\mathbf{h}} = [\bar{\mathrm{h}}_{\mathbb{D}_1}, \cdots, \bar{\mathrm{h}}_{\mathbb{D}_{2D-1}}]^{\mathrm{T}}$ whose uth elements, $u \in [1, 2, \cdots, (2D-1)]$, are respectively expressed as

$$\mathrm{h}_{\mathbb{D}_u} = \frac{1}{\sqrt{1 - \left| \mathcal{R}\left(\sum_{l=1}^{L} \bar{\sigma}_l{}^2 e^{-\jmath \langle \mathbb{D} \rangle_u \pi \sin \theta_l} \right) \right|^2}} \tag{55}$$

and

$$\bar{\mathrm{h}}_{\mathbb{D}_u} = \frac{1}{\sqrt{1 - \left| \mathcal{I}\left(\sum_{l=1}^{L} \bar{\sigma}_l{}^2 e^{-\jmath \langle \mathbb{D} \rangle_u \pi \sin \theta_l} \right) \right|^2}}. \tag{56}$$

Similarly, substituting (52)–(54) into (41)–(44) renders the FIM and the CRB for the one-bit data case.

5.5. CRB and FIM for Mixed-Precision Data Model

Now we consider the CRB of the array when mixed-precision data are utilized. Define two binary mask matrices $\mathbf{\Gamma} = \mathrm{bdiag}(\mathbf{1}_{M_1}, \cdots, \mathbf{1}_{M_K})$ and $\bar{\mathbf{\Gamma}} = \mathbf{1}_M - \mathbf{\Gamma}$ such that $\mathbf{\Gamma} \circ \mathbf{R} = \mathbf{\Gamma} \circ \mathbf{R}_{\mathrm{FP}}$ contains the self-covariance matrices associated with the full-precision data and $\bar{\mathbf{\Gamma}} \circ \mathbf{R} = \bar{\mathbf{\Gamma}} \circ \mathbf{R}_{1\mathrm{B}}$ contains the cross-covariance matrices associated with the one-bit data. As such, the mixed-precision covariance matrix $\mathbf{R}$ can be expressed as

$$\mathbf{R} = \mathbf{\Gamma} \circ \mathbf{R} + \bar{\mathbf{\Gamma}} \circ \mathbf{R} = \mathbf{\Gamma} \circ \mathbf{R}_{\mathrm{FP}} + \bar{\mathbf{\Gamma}} \circ \mathbf{R}_{1\mathrm{B}}. \tag{57}$$

In order to compute the FIM components $\mathbf{\Delta}_{\boldsymbol{\omega}}$ and $\mathbf{\Delta}_{\mathbf{o}}$, which are respectively defined in (42) and (43) and correspond to the full-precision and one-bit data, we can use the results developed in Sections 5.3 and 5.4 respectively for the full-precision and one-bit data models. For clarity, we use the superscripts FP, MP, and 1B to denote the FIM components corresponding to the full-precision, mixed-precision, and one-bit data models, respectively. By further denoting $\mathbf{\Gamma}_{\mathrm{E}} = \mathrm{diag}[\mathrm{vec}(\mathbf{\Gamma})]$ and $\bar{\mathbf{\Gamma}}_{\mathrm{E}} = \mathrm{diag}[\mathrm{vec}(\bar{\mathbf{\Gamma}})]$, the two FIM components corresponding to the mixed-precision data model are respectively computed as

$$\mathbf{\Delta}_{\boldsymbol{\omega}}^{\mathrm{MP}} = \mathbf{\Gamma}_{\mathrm{E}} \mathbf{\Delta}_{\boldsymbol{\omega}}^{\mathrm{FP}} + \bar{\mathbf{\Gamma}}_{\mathrm{E}} \mathbf{\Delta}_{\boldsymbol{\omega}}^{1\mathrm{B}} \tag{58}$$

and

$$\mathbf{\Delta}_{\mathbf{o}}^{\mathrm{MP}} = \mathbf{\Gamma}_{\mathrm{E}} \mathbf{\Delta}_{\mathbf{o}}^{\mathrm{FP}} + \bar{\mathbf{\Gamma}}_{\mathrm{E}} \mathbf{\Delta}_{\mathbf{o}}^{1\mathrm{B}}. \tag{59}$$

Incorporating equations (58) and (59) into equation (44) leads to the calculation of the CRB for the sparse distributed array in the mixed-precision data scenario.
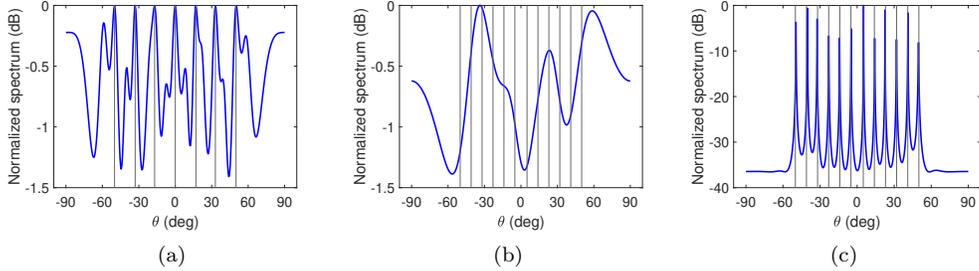
Figure 3: MUSIC pseudo-spectra based on self- and cross-covariance matrices with full precision data. (a) No interpolation, 7 sources, (b) No interpolation, 12 sources (c) With interpolation, 12 sources.
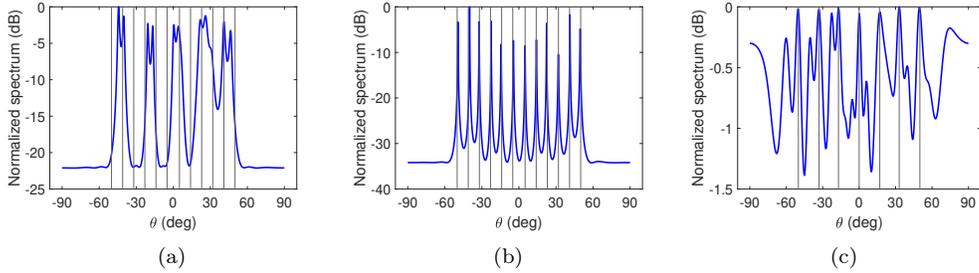

Figure 4: MUSIC pseudo-spectra based on self-covariance matrices only or one-bit data for cross-covariance matrix computations. (a) No cross-covariance elements, with interpolation, 12 sources, (b) Mixed-precision data, with interpolation, 12 sources, (c) One-bit data, no interpolation, 7 sources.

It is important to note that the existence of the CRB is contingent upon the FIM being non-singular [55]. It can be deduced from the preceding expressions that this requirement can be met when both the full-precision and one-bit FIMs are non-singular.

6. Numerical Results

Consider a distributed array consisting of three subarrays, and each subarray consists of 3 sparsely placed sensors. In the default array configuration, the three subarrays have distinct sensor placement patterns, respectively given as

$$\mathbb{S}_1 = \{0, 1, 4\}d, \quad \mathbb{S}_2 = \{7, 9, 11\}d, \quad \mathbb{S}_3 = \{16, 19, 21\}d.$$

The distributed array configuration is shown in Fig. 1. In this case, all array sensors are aligned with the half-wavelength grid.

6.1. Comparison of MUSIC Pseudo-Spectra

We consider two scenarios, respectively with 7 and 12 uncorrelated sources that are uniformly distributed between $-50°$ and $50°$. We use $T = 200$ data snapshots at each subarray and the input SNR is set to 0 dB.

As a benchmark for comparison, we first consider the DOA estimation problem where all sensors use full-precision data without quantization. In Fig. 3(a), the MUSIC pseudo-spectrum of the DOA estimates is shown for $L = 7$ sources without performing covariance matrix interpolation. In this case, since the number of sources is smaller than the number of the total number of sensors and no interpolation is performed, all source locations are determined with a root mean-square error (RMSE) of $0.084°$. However, due to the holes in the correlation lags, high sidelobes are observed in the spectrum.

On the other hand, when $L = 12$ which is higher than the total number of sensors, the MUSIC spectrum fails to locate the sources, as depicted in Fig. 3(b). In Fig. 3(c), we consider the scenario when matrix completion is performed to interpolate the correlation results. In this case, the correlation results for all lags between 0 and 21 are obtained and, as a result, all the 12 sources are resolved with an RMSE of $0.314°$.

Next, we consider the scenario in which no raw or one-bit data are exchanged between the subarrays and the processing center. Rather, each subarray only reports its self-covariance matrix to the processing center. In this case, the covariance matrix of the whole array observed at the processing center is block-diagonal, as all the cross-covariance elements are missing. It is interesting to note that, while matrix completion is still possible based on the self-covariance matrices [59], the source directions are unresolved as a result of the missing off-block-diagonal elements in the resulting covariance matrix. The MUSIC pseudo-spectrum obtained for the 12-source scenario is shown in Fig. 4(a) which does not indicate the correct DOA estimates.

When one-bit quantized data are transmitted from the subarrays to the processing center and used for the computation of cross-covariance entries, the DOA estimation performance using the resulting mixed-precision covariance matrix is only slightly inferior to the full-precision case. Fig. 4(b) depicts the MUSIC pseudo-spectrum for the 12-source scenario after performing
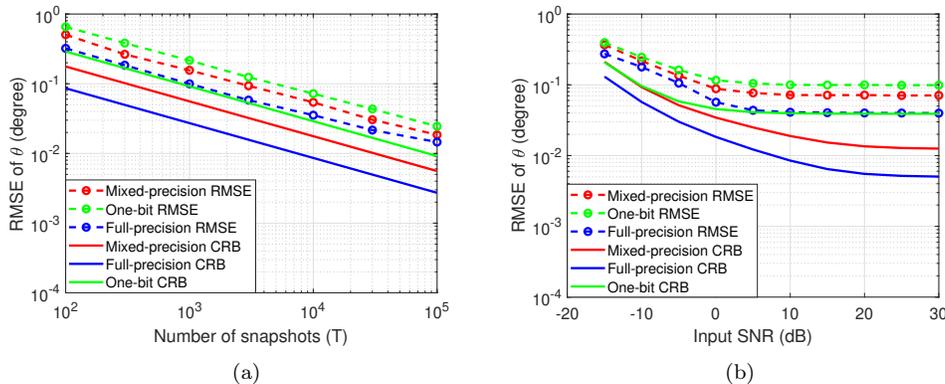
Figure 5: (a) RMSE and CRB versus number of snapshots ($\epsilon_k = 0$, input SNR = 5 dB). (b) RMSE and CRB versus input SNR (dB) ($\epsilon_k = 0$, $T = 5{,}000$ snapshots).

matrix completion, and the corresponding RMSE is 0.491°. When matrix interpolation is not carried out, similar to what we considered in Fig. 3(a), the array with 9 physical sensors does not recognize more than 8 sources. Fig. 4(c) shows the results of the mixed-precision array for the 7-source scenario without performing interpolation. In this case, the RMSE is 0.176°.

In the simulation results that follow, we focus on the results with 10 sources uniformly distributed between −50° and 50°, and covariance matrix completion is performed in all cases. Except in Section 6.3, the default array is used and no off-grid subarray displacements are considered.

6.2. Comparison of CRB and RMSE Performance

The CRB and RMSE performance of the distributed array is depicted in Fig. 5(a) with respect to the number of snapshots. The RMSE results are computed from 200 independent trials and covariance matrix completion is performed. It is found in this figure that the mixed-precision processing offers a significant improvement over the one-bit data case, even though it is inferior to the full-precision data case due to one-bit quantization in reconstructing the cross-covariance elements. Similar results are observed in Fig. 5(b) which shows the CRB and RMSE curves with respect to the input SNR of the signals.

Fig. 6 shows the CRB with respect to the number of sources, L. Noted that the maximum number of sources that can be detected by the distributed array is 20 because there are 21 sensors in the interpolated array. It is
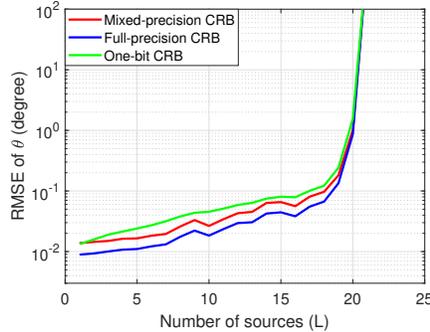
25

Figure 6: CRB versus number of sources ($\epsilon_k = 0$, input SNR $= 5$ dB, $T = 5{,}000$ snapshots).

observed in Fig. 6 that the CRB increases sharply When more than 20 sources are present.

6.3. Effect of Off-Grid Subarray Positions

So far, we have focused on the default distributed array in which all the subarrays are on the half-wavelength grid, i.e., $\epsilon_k = 0$ for all subarrays. In this subsection, we consider the case in which the second subarray (i.e., $k = 2$) is displaced from the on-grid location by $\epsilon_2 = 0.2d$. To estimate the source DOAs in this scenario, we employ the iterative DOA estimation approach described in Section 4.

In Fig. 7, we show the convergence performance of the iterative method. The solid curves in Fig. 7 show the performance of the proposed iterative method for DOA estimation in the case of $\epsilon_2 = 0.2d$, where the first iteration represents the results before applying the iterative method. It is observed that the iterative method improves the performance in the underlying off-grid subarray displacement scenario. The RMSE does not significantly change after the second iteration, implying the fast convergence of this approach. This is because the effect due to the phase offset, expressed in $\mathbf{\Phi}_{k_1 k_2}$, is adequately compensated for in the second iteration, and increased iterations does not further improve the estimates of the source covariance matrix $\hat{\mathbf{S}}$. For comparison, the dashed lines in Fig. 7 show the RMSE corresponding to the same parameters as the solid lines of the same color when the subarray does not have off-grid displacement (i.e., $\epsilon_2 = 0$).

Fig. 8 compares the RMSE performance after convergence. As illustrated in Fig. 8(a), the full-precision data model achieves the best performance, whereas the mixed-resolution model detects all sources with a significantly
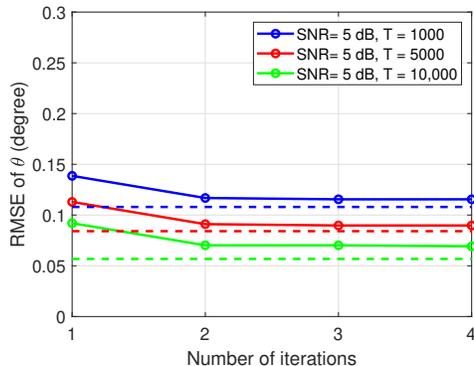
26

Figure 7: Mixed precision RMSE versus number of iterations (solid lines: $\epsilon_2 = 0.2d$; dashed lines: $\epsilon_2 = 0$).

low RMSE than the one-bit counterpart with using the full-precision self-covariance matrices. Similar trends can also be observed in Fig. 8(b) where the RMSE is plotted with respect to the varying input SNR.

In order to better demonstrate the significance of the proposed iterative method, we present the RMSE of the estimated DOAs for different subarray displacement scenarios as shown in Fig. 9. The CRB is also included for reference. It is observed in Fig. 9(a) that, when the proposed iterative algorithm is not used, the RMSE values become even higher for the $\epsilon_2 = 0.5d$ case compared to that of the $\epsilon_2 = 0.2d$ case. On the other hand, when the iterative algorithm is employed, the RMSE values corresponding to the two cases become very close, demonstrating the effectiveness of the proposed algorithm to alleviate the effects due to subarray displacements. Similar results can be observed in Fig. 9(b) when the RMSE is depicted with respect to the input SNR.

6.4. Comparison of Required Data Bits

In the previous subsections, it has been shown how the RMSE performance of the estimated DOAs varies with respect to the number of available snapshots and the input SNR. In this subsection, we compare the performance in terms of the number of data bits being transferred between the subarrays and the processing center. In particular, it is shown that, when the same number of data bits is used, the proposed mixed-precision data model achieves the best performance compared to the full-precision and one-bit data cases.
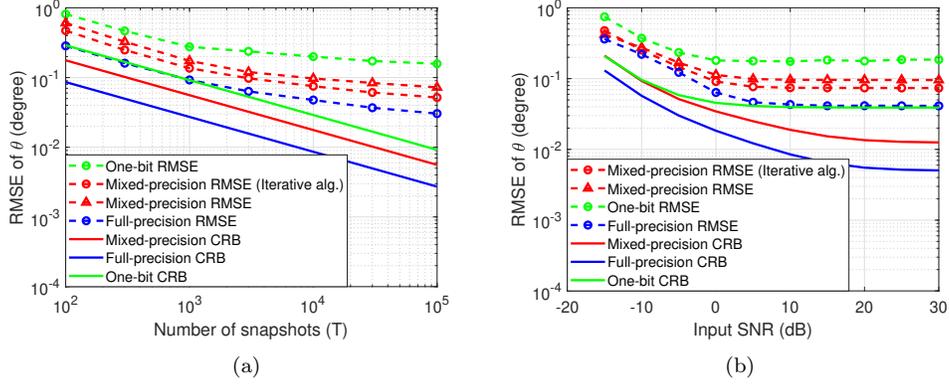
Figure 8: (a)RMSE and CRB versus number of snapshots (input SNR = 5 dB, $\epsilon_2 = 0.2d$) (b) RMSE and CRB versus input SNR (dB) ($T = 5,000$ snapshots, $\epsilon_2 = 0.2d$).
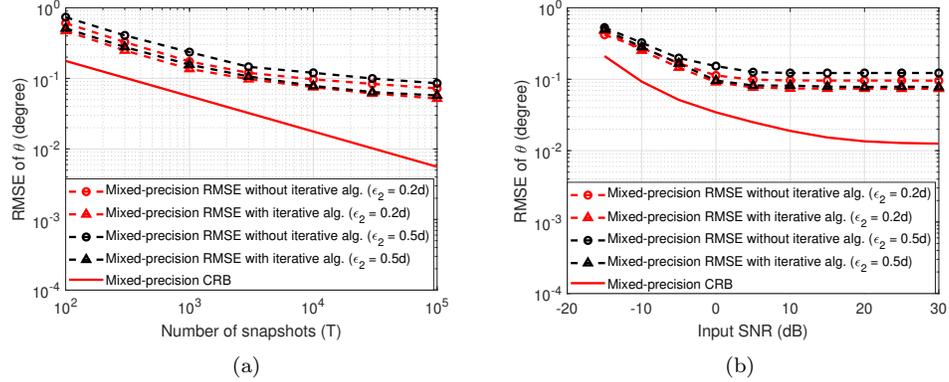

Figure 9: Comparison of RMSE for different subarray displacement scenarios ($\epsilon_2 = 0.2d$ and $\epsilon_2 = 0.5d$) with and without performing the proposed iterative algorithm. (a) RMSE and CRB versus the number of snapshots (input SNR = 5 dB) (b) RMSE and CRB versus the input SNR (dB) ($T = 5,000$ snapshots).
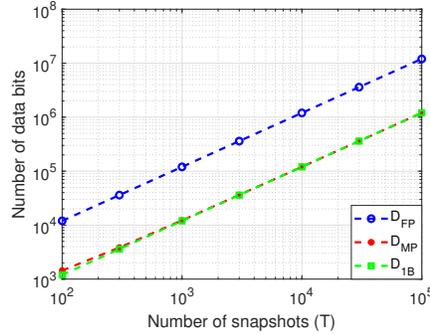
Figure 10: Number of data bits versus number of snapshots (input SNR $= 5$ dB).

Consider that D-bit data are used to express the full-precision data. The number of bits required for the full-precision model is

$$\mathrm{D_{FP}} = M \, \text{sensors} \times T \, \text{snapshots} \times D \, \text{bits} \times 2 \, \text{components}$$
$$= 2MTD \, \text{bits}.$$

As an example, when $M = 9$ sensors, $T = 1,000$ snapshots, and $D = 10$ bits, the resulting $\mathrm{D_{FP}}$ is 18,000 bits. More bits are required is a higher number of bits are used to represent full-precision data.

For the one-bit model, the number of required bits can be obtained as

$$\mathrm{D_{1B}} = M \, \text{sensors} \times T \, \text{snapshots} \times 1 \, \text{bit} \times 2 \, \text{components}$$
$$= 2MT \, \text{bits}.$$

For the same example, it renders $\mathrm{D_{1B}} = 1,800$ bits.

Now for the mixed-precision model, the data bits required can be formulated as the summation of the data required for the one-bit model, and the upper triangular portion of the self-covariance matrices. Because the self-covariance matrix is Hermitian with identical diagonal entries, ignoring any redundant entries due to same lag pairs, the number of unique entries in the kth subarray with M_k elements is $M_k(M_k - 1)/2 + 1$. Therefore, the total number of data bits to be transmitted from the subarrays to the processing center is

$$\mathrm{D_{MP}} = \mathrm{D_{1B}} + 2D \sum_{k=1}^{K} \left[\frac{M_k \left(M_k - 1 \right)}{2} + 1 \right] \text{bits}.$$

For the underlying example, we obtain $\mathrm{D_{MP}}$ to be $2,040$ bits. This is only 240 more bits or 13.3% higher than the one-bit case but achieves 88.67% of
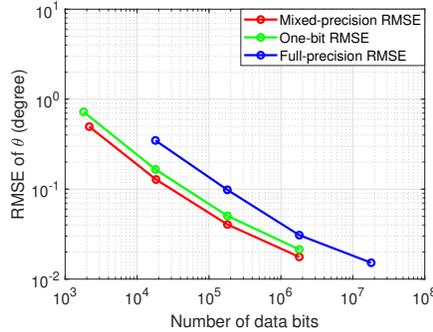
Figure 11: RMSE versus number of data bits (input SNR = 5 dB).

reduction of the data bits compared to that required for the full-precision model.

Fig. 10 demonstrates how the data bits required for the three data models vary with increasing number of snapshots. It can be inferred from the figure that at high snapshot scenarios, the number of bits required for the mixed-precision model approaches closer to that of the one-bit model. For example, when T is increased to 10^4 snapshots, the required number of bits for the full-precision, mixed-precision, and one-bit models are respectively 180,000 bits, 18,000 bits, and 18,240 bits. The mixed-precision model still requires 240 bits higher than the one-bit model, but the ratio is reduced to 1.33%. On the other hand, the reduction from the full-precision model reaches 89.87%.

Fig. 11 compares the RMSE performance achieved with respect to the number of data bits. The number of data bits depicted in the figure corresponds to the scenarios associated with $T = 10^2, 10^3, 10^4$, and 10^5 snapshots. For a given T, the number of bits required for the full-precision model is much higher, whereas the one-bit and mixed-precision data models require a much lower number of data bits. As a result, for a given number of data bits, the mixed-precision model achieves the lowest RMSE, thus demonstrating the superiority of the proposed mixed-precision model, making the proposed approach attractive in a traffic-limited network.

7. Conclusion

In this paper, we considered the DOA estimation problem exploiting collaborative distributed arrays to resolve a high number of sources which may exceed the total number of distributed sensors. The key contribution of

this paper is the development of mixed-precision covariance matrices in the distributed array that leverage the full potential of distributed arrays while minimizing communication traffic between the subarrays and the processing center. The required data traffic of the proposed technique is comparable to the one-bit data case, but the utilization of the full-precision subarray self-covariance matrices enables high-performance DOA estimation. In particular, in a traffic-limited network, the proposed technique based on mixed-precision covariance matrices achieves the highest DOA estimation performance. We also considered the scenario in which subarrays are not aligned in the half-wavelength grid, and an iterative DOA estimation method was developed to ensure robust DOA estimation.

8. References

[1] Y. D. Zhang and A. Prater-Bennette, "Collaborative direction-of-arrival estimation exploiting one-bit cross-correlations," in *Proc. Asilomar Conf. Signals, Syst. Comput.*, Pacific Grove, CA, Nov. 2021, pp. 236–240.

[2] M. W. T. S. Chowdhury and Y. D. Zhang, "Cramér-Rao bound analysis of distributed DOA estimation exploiting mixed-precision covariance matrix," in *Proc. IEEE Int. Conf. Acoust., Speech and Signal Process. (ICASSP)*, Singapore, May 2022, pp. 5163–5167.

[3] H. L. Van Trees, *Optimum Array Processing: Part IV of Detection, Estimation, and Modulation Theory*. Wiley, 2002.

[4] E. Tuncer and B. Friedlander (eds), Classical and Modern Direction of Arrival Estimation. Academic Press, 2009.

[5] A. Leshem and A.-J. van der Veen, "Radio-astronomical imaging in the presence of strong radio interference," *IEEE Trans. Inform. Theory*, vol. 46, no. 5, pp. 1730–1747, Aug. 2000.

[6] L. Zhao, X. Li, L. Wang, and G. Bi, "Computationally efficient wide-band DOA estimation methods based on sparse Bayesian framework," *IEEE Trans. Vehi. Tech.*, vol. 66, no. 12, pp. 11108–11121, Dec. 2017.

[7] A. Ryan, M. Zennaro, A. Howell, R. Sengupta, and J. Hedrick, "An overview of emerging results in cooperative UAV control," in *Proc. IEEE Conf. Decision and Control*, Bahamas, Dec. 2004, pp. 602–607.

[8] D. Cole, A. Goktogan, P. Thompson, and S. Sukkarieh, "Mapping and tracking," *IEEE Robot. Autom. Mag.*, vol. 16, no. 2, pp. 22–34, June 2009.

[9] X. Li and Y. D. Zhang, "Multi-source cooperative communications using multiple small relay UAVs," in *Proc. IEEE Globecom Workshop on Wireless Networking for Unmanned Aerial Vehicles*, Miami, FL, Dec. 2010, pp. 1805–1810.

[10] B. K. Chalise, Y. D. Zhang, and M. G. Amin, "Multi-beam scheduling for unmanned aerial vehicle networks," in *Proc. IEEE/CIC Int. Conf. Commun. in China*, Xi'an, China, Aug. 2013, pp. 442–447.

[11] S. Hayat, E. Yanmaz, and R. Muzaffar, "Survey on unmanned aerial vehicle networks for civil applications: A communications viewpoint," *IEEE Commun. Surveys Tut.*, vol. 18, no. 4, pp. 2624–2661, 2016.

[12] E. Yanmaz, S. Yahyanejad, B. Rinner, H. Hellwagner, and C. Bettstetter, "Drone networks: Communications, coordination, and sensing," *Ad Hoc Networks*, vol. 68, pp. 1–15, Jan. 2018.

[13] P. Stoica, A. Nehorai, and T. Söderström, "Decentralized array processing using the MODE algorithm," *Circuits, Syst. Signal Process.*, vol. 14, no. 1, pp. 17—38, 1995.

[14] M. Pesavento, A. B. Gershman, and K. M. Wong, "Direction finding in partly calibrated sensor arrays composed of multiple subarrays," *IEEE Trans. Signal Process.*, vol. 50, no. 9, pp. 2103–2115, Sept. 2002.

[15] W. Suleiman, P. Parvazi, M. Pesavento, and A. M. Zoubir, "Non-coherent direction-of-arrival estimation using partly calibrated arrays," *IEEE Trans. Signal Process.*, vol. 66, no. 21, pp. 5776–5788, Nov. 2018.

[16] M. W. T. S. Chowdhury and Y. D. Zhang, "Direction-of-arrival estimation exploiting distributed sparse arrays," in *Proc. Asilomar Conf. Signals, Syst. Comput.*, Pacific Grove, CA, Nov. 2021, pp. 231–235.

[17] A. Ahmed, S. Zhang, and Y. D. Zhang, "Multi-target motion parameter estimation exploiting collaborative UAV network," in *Proc. IEEE Int. Conf. Acoust., Speech and Signal Process. (ICASSP)*, Brighton, UK, May 2019, pp. 4459–4463.

[18] C. Liang, Y. Wang, Z. Yang, X. Hu, Q. Pei, W. Gu, and L. Zhang, "Cooperative automotive radars with multi-aperture multiplexing MIMO sparse array design." *Electronics*, vol. 11, no. 1198, pp. 1–20, 2022.

[19] A. Moffet, "Minimum-redundancy linear arrays," *IEEE Trans. Antennas Propagat.*, vol. 16, no. 2, pp. 172–175, March 1968.

[20] R. T. Hoctor and S. A. Kassam, "The unifying role of the co-array in aperture synthesis for coherent and incoherent imaging," *Proc. IEEE*, vol. 78, no. 4, pp. 735–752, April 1990.

[21] P. Pal and P. P. Vaidyanathan, "Nested arrays: A novel approach to array processing with enhanced degrees of freedom," *IEEE Trans. Signal Process.*, vol. 58, no. 8, pp. 4167–4181, Aug. 2010.

[22] P. P. Vaidyanathan and P. Pal, "Sparse sensing with co-prime samplers and arrays," *IEEE Trans. Signal Process.*, vol. 59, no. 2, pp. 573–586, Feb. 2011.

[23] S. Qin, Y. D. Zhang, and M. G. Amin, "Generalized coprime array configurations for direction-of-arrival estimation," *IEEE Trans. Signal Process.*, vol. 63, no. 6, pp. 1377–1390, March 2015.

[24] A. Ahmed and Y. D. Zhang, "Generalized non-redundant sparse array designs," *IEEE Trans. Signal Process.*, vol. 69, pp. 4580–4594, Aug. 2021.

[25] O. Bar-Shalom and A. J. Weiss, "DOA estimation using one-bit quantized measurements," *IEEE Trans. Aerosp. Electronic Syst.*, vol. 38, no. 3, pp. 868–884, July 2002.

[26] S. Jacobsson, G. Durisi, M. Coldrey, U. Gustavsson, and C. Studer, "One-bit massive MIMO: Channel estimation and high-order modulations," in *Proc. IEEE Int. Conf. Commun. Workshop (ICCW)*, London, U.K., June 2015, pp. 1304–1309.

[27] K. Yu, Y. D. Zhang, M. Bao, Y.-H. Hu, and Z. Wang, "DOA estimation from one-bit compressed array data via joint sparse representation," *IEEE Signal Process. Lett.*, vol. 23, no. 9, pp. 1279–1283, Sept. 2016.

[28] C. Liu and P. P. Vaidyanathan, "One-bit sparse array DOA estimation," in *Proc. IEEE Int. Conf. Acoust., Speech and Signal Process. (ICASSP)*, New Orleans, LA, pp. 3126–3130, 2017.

[29] X. Huang and B. Liao, "One-bit MUSIC," *IEEE Signal Process. Lett.*, vol. 26, no. 7, pp. 961–965, July 2019.

[30] A. Ameri, A. Bose, J. Li, and M. Soltanalian, "One-bit radar processing with time-varying sampling thresholds," *IEEE Trans. Signal Process.*, vol. 67, no. 20, pp. 5297–5308, Oct. 2019.

[31] T. Chen, M. Guo, and X. Huang, "Direction finding using compressive one-bit measurements," *IEEE Access*, vol. 6, pp. 41201–41211, 2018.

[32] H. Qiao and P. Pal, "Gridless line spectrum estimation and low-rank Toeplitz matrix compression using structured samplers: A regularization-free approach," *IEEE Trans. Signal Process.,* vol. 65, no. 9, pp. 2221–2236, May 2017.

[33] X. Wu, W.-P. Zhu, and J. Yan, "A Toeplitz covariance matrix reconstruction approach for direction-of-arrival estimation," *IEEE Trans. Veh. Technol.,* vol. 66, no. 9, pp. 8223–8237, Sep. 2017.

[34] C. Zhou, Y. Gu, Z. Shi, and Y. D. Zhang, "Off-grid direction-of-arrival estimation using coprime array interpolation," *IEEE Signal Process. Lett.*, vol. 25, no. 11, pp. 1710–1714, Nov. 2018.

[35] C. Zhou, Y. Gu, X. Fan, Z. Shi, G. Mao, and Y. D. Zhang, "Direction-of-arrival estimation for coprime array via virtual array interpolation," *IEEE Trans. Signal Process.,* vol. 66, no. 22, pp. 5956–5971, Nov. 2018.

[36] S. Zhang, A. Ahmed, Y. D. Zhang, and S. Sun, "DOA estimation exploiting interpolated multi-frequency sparse array," in *Proc. IEEE Sensor Array and Multichannel Signal Process. Workshop*, Hangzhou, China, June 2020, pp. 1–5.

[37] S. Liu, Z. Mao, Y. D. Zhang, and Y. Huang, "Rank minimization-based Toeplitz reconstruction for DoA estimation using coprime array," *IEEE Commun. Lett.*, vol. 25, no. 7, pp. 2265–2269, July 2021.

[38] D. Castanheira and A. Gameiro, "Low complexity and high-resolution line spectral estimation using cyclic minimization," *IEEE Trans. Signal Process.*, vol. 67, no. 24, pp. 6285–6300, Dec. 2019.

[39] S. Sun and Y. D. Zhang, "4D automotive radar sensing for autonomous vehicles: A sparsity-oriented approach," *IEEE Sel. Topics Signal Process.*, vol. 15, no. 4, pp. 879–891, June 2021.

[40] C. Zhou, Y. Gu, Y. D. Zhang, and Z. Shi, "Sparse array interpolation for direction-of-arrival estimation," in M. G. Amin (ed.), *Sparse Arrays for Radar, Sonar, and Communications*, Wiley-IEEE Press, 2024.

[41] R. Schmidt, "Multiple emitter location and signal parameter estimation," *IEEE Trans. Antennas Propagat.*, vol. 34, no. 3, pp. 276–280, March 1986.

[42] L. Wang, C. Ren, R. Liu, and Z. Zheng, "Direction-of-arrival estimation for nested array using mixed-resolution ADCs," *IEEE Commun. Lett.*, May 2022, pp. 1868–1872.

[43] B. Shi, R. Dong, Q. Jie, L. Zhu, F. Shu, and J. Wang, "DOA estimation for hybrid massive MIMO systems using mixed-ADCs: Performance loss and energy efficiency," *IEEE Open J. Commun. Soc.*, vol. 4, pp. 1383–1395, 2023.

[44] L. Wang, C. Ren, and Z. Zheng, "DOA estimation for monostatic coprime MIMO radar with mixed-resolution quantization," *IEEE Trans. Vehi. Tech.*, in press, doi: 10.1109/TVT.2023.3293135.

[45] J. Shi, F. Wen, and T. Liu, "Nested MIMO Radar: Coarrays, Tensor Modeling, and Angle Estimation," *IEEE Trans. Aero. Electron. Sys.*, vol. 57, no. 1, pp. 573-585, Feb. 2021.

[46] S. Sedighi, M. R. B. Shankar, M. Soltanalian, and B. Ottersten, "On the performance of one-bit DoA estimation via sparse linear arrays," *IEEE Trans. Signal Process.*, vol. 69, pp. 6165–6182, 2021.

[47] J. H. Van Vleck and D. Middleton, "The spectrum of clipped noise," *Proc. IEEE*, vol. 54, no. 1, pp. 2–19, Jan. 1966.

[48] Y. Li, C. Tao, G. Seco-Granados, A. Mezghani, A. L. Swindlehurst, and L. Liu, "Channel estimation and performance analysis of one-bit massive MIMO systems," *IEEE Trans. Signal Process.*, vol. 65, no. 15, pp. 4075–4089, Aug. 2017.

[49] S. Redif, J. G. McWhirter, and S. Weiss, "Design of FIR paraunitary filter banks for subband coding using a polynomial eigenvalue decomposition," *IEEE Trans. Signal Process.*, vol. 59, no. 11, pp. 5253--5264, Nov. 2011.

[50] B. A. Karim and H. K. Ali, "Computationally efficient MUSIC based DOA estimation algorithm for FMCW radar," *J. Electronic Science Tech.*, vol. 21, no, 1, pp. 1–18, 2023.

[51] K. Liu and Y. D. Zhang, "Coprime array-based robust beamforming using covariance matrix reconstruction technique," *IET Commun.*, vol. 12, no. 17, pp. 2206–2212, Oct. 2018.

[52] I. Abrahamson, "Orthant probabilities for the quadrivariate normal distribution," *Ann. Math. Stat*, vol. 35, no. 4, pp. 1685–1703, 1964.

[53] P. Stoica and P. Babu, "The Gaussian data assumption leads to the largest Cramér-Rao bound," *IEEE Signal Process. Mag.*, vol. 28, no. 3, pp. 132-–133, 2011.

[54] M. Jansson, B. Goransson, and B. Ottersten, "A subspace method for direction of arrival estimation of uncorrelated emitter signals," *IEEE Trans. Signal Process.*, vol. 47, no. 4, pp. 945–956, April 1999.

[55] C.-L. Liu and P. P. Vaidyanathan, "Cramér-Rao bounds for coprime and other sparse arrays, which find more sources than sensors," *Digital Signal Process.*, vol. 61, pp. 43–61, 2017.

[56] P. Stoica and A. Nehorai, "MUSIC, maximum likelihood, and Cramér-Rao bound," *IEEE Trans. Acoust., Speech, Signal Process.*, vol. 37, no. 5, pp. 720–741, May 1989.

[57] P. Stoica, E. G. Larsson, and A. B. Gershman, "The stochastic CRB for array processing: a textbook derivation," *IEEE Signal Process. Lett.*, vol. 8, no. 5, pp. 148–150, May 2001.

[58] A. Weiss and B. Friedlander, "On the Cramér-Rao bound for direction finding of correlated signals," *IEEE Trans. Signal Process.*, vol. 41, no. 1, pp. 495–499, Jan. 1993.

[59] L. Yu, J. Antoni, Q. Leclere, and W. Jiang, "Acoustical source reconstruction from non-synchronous sequential measurements by fast iterative shrinkage thresholding algorithm," *J. Sound Vib.*, vol. 408, pp. 351–367, 2017.